Subwavelength imaging of light by arrays of metal-coated semiconductor nanoparticles: a theoretical study

2008 J. Phys.: Condens. Matter 20 255201

(http://iopscience.iop.org/0953-8984/20/25/255201)

IOP PUBLISHING JOURNAL OF PHYSICS: CONDENSED MATTER

J. Phys.: Condens. Matter **20** (2008) 255201 (8pp) doi:10.1088/0953-8984/20/25/255201

Subwavelength imaging of light by arrays of metal-coated semiconductor nanoparticles: a theoretical study

Vassilios Yannopapas

Department of Materials Science, University of Patras, GR-26504 Patras, Greece

E-mail: vyannop@upatras.gr

Received 15 January 2008, in final form 20 April 2008
Published 19 May 2008
Online at stacks.iop.org/JPhysCM/20/255201

Abstract

Rigorous calculations of the imaging properties of metamaterials consisting of metal-coated semiconductor nanoparticles are presented. In particular, it is shown that under proper choice of geometric and material parameters, arrays of such particles exhibit negative refractive index within the region of the excitonic resonance of the semiconductor. The occurrence of negative refractive index is predicted by the extended Maxwell–Garnett theory and confirmed by a layer-multiple scattering method for electromagnetic waves. By using the same method it is shown that within the negative refractive index band arrays of such nanoparticles amplify the transferred near-field while simultaneously narrowing down its spatial profile, leading to subwavelength resolution. The effect of material losses on the imaging properties of the arrays is also addressed.

(Some figures in this article are in colour only in the electronic version)

1. Introduction

According to a recent definition [1], metamaterials are artificial materials which exhibit response characteristics that are not observed in the individual responses of its constituent materials. The most fascinating class of metamaterials are those exhibiting simultaneously negative permittivity ϵ and permeability μ, i.e. a negative refractive index (NRI) [2, 3]. These materials are also known as left-handed metamaterials (LHMs) since, within their volume, the electric-field the magnetic-field and the wavevector form a left-handed triad. The usual approach of designing a LHM is to combine a 'magnetic' sublattice (one which exhibits negative μ) of miniaturized resistance–inductance–capacitance (RLC) circuits, e.g. split-ring resonators, with an 'electric' one (exhibiting negative ϵ) of thin metallic wires [4]. However, an alternative route has been recently suggested where the electric and magnetic sublattices are occupied by units of less elaborate geometry such as cylinders or spheres made from resonant materials (ionic, semiconducting or plasmonic materials) displaying high refractive index within a specific frequency window [5–14]. The magnetic activity of the cylinders/spheres lies within the region of Mie resonances resulting from the enhancement of the displacement current inside each sphere which, in turn, gives rise to a macroscopic magnetization of the whole structure. The electric activity is attributed to the large polarization induced by the sphere due to the giant dielectric permittivity around the resonance frequency of a given dielectric function, e.g. polariton, plasmon or exciton resonance. The above theoretical suggestions have been recently verified experimentally for arrays of dielectric particles of millimeter [15] and micrometer [16] size. Such arrays can be miniaturized to the nanometer scale in the form of nanoparticle superlattices [17].

Perhaps, the most paramount application of LHMs is using their imaging properties; as has been pioneered by Pendry [3] and verified experimentally, a planar slab of metamaterial with NRI can overcome the standard diffraction limit in imaging by focusing the far-field via negative refraction [18, 19] and by amplifying the near-field [20–22] by surface-plasmon excitation, a possibility which promises the realization of a perfect lens. Near-field amplification is also feasible separately for S-polarized waves in the magnetostatic limit using solely RLC circuits such as split-ring resonators and Swiss rolls [23, 24] and for P-polarized waves in the electrostatic limit using periodic structures with metallic components such as rods [25], wires [26], and spheres [27].

In this work we study the imaging properties of three-dimensional (3D) LHMs consisting of metal-coated semiconductor spheres. As has been recently shown, arrays of semiconductor spheres with strong excitonic oscillation strength (CuCl, Cu_2O) can exhibit negative permeability in the visible region, around the exciton resonance [13]. In order to realize an LHM in the regime of negative μ, the array of semiconductor spheres can be (a) either combined with an array of metallic spheres (negative ϵ) in a way that a binary LHM is created [8], or (b) by coating the semiconductor spheres with a metallic shell [10, 28]. The above structures have been studied by employing both effective medium treatments [6, 11, 12] and more rigorous electromagnetic approaches [8, 10]. By exploiting the occurrence of NRI in the case of arrays of metal-coated semiconductor nanoparticles, we will show that near-field amplification along with subwavelength resolution of an image can be achieved in such structures, for both polarization modes. We will also elucidate the role of absorption which is intrinsic in the materials constituting the LHM under study. The paper is organized as follows. In section 2 the basic theoretical tools for studying the imaging properties of arrays of spherical inclusions is presented. Section 3 applies the theory to the case of metal-coated semiconductor spheres and section 4 concludes the paper.

2. Theory

In this work, we are dealing with finite slabs of metamaterials consisting of a number of planes of spheres with the same two-dimensional (2D) periodicity. In order to probe the imaging properties of these structures, we consider the electric-field emitted by a localized source, namely, that radiated by a small, linear, infinitely thin, center-fed antenna. The antenna lies along the z-axis from $-d/2 \leqslant z \leqslant d/2$ with current I. We expand the electric-field radiated by the antenna as a series of spherical waves [29]

$$\mathbf{E}(\mathbf{r}) = \sum_{l=1}^{\infty}\sum_{m=-l}^{l}\left\{a_{Hlm}h_l^+(qr)\mathbf{X}_{lm}(\hat{\mathbf{r}}) + a_{Elm}\frac{\mathrm{i}}{q}\nabla\times\left[h_l^+(qr)\mathbf{X}_{lm}(\hat{\mathbf{r}})\right]\right\}, \quad (1)$$

$\mathbf{X}_{lm}(\hat{\mathbf{r}})$ are the so-called vector spherical harmonics [29] and h_l^+ are the spherical Hankel functions of order l. $q = \omega/c$, where $c = 1/\sqrt{\mu\epsilon\mu_0\epsilon_0} = c_0/\sqrt{\mu\epsilon}$ is the velocity of light in the medium surrounding the antenna. The magnetic multipole coefficients a_{Hlm} are zero whilst the electric ones are given by [30]

$$a_{Elm} = \frac{I}{\pi d}\sqrt{\frac{4\pi(2l+1)}{l(l+1)}}\left(\frac{qd}{2}\right)^2 j_l\left(\frac{qd}{2}\right) \quad (2)$$

provided that l is odd and $m = 0$. j_l in equation (2) denote the spherical Bessel functions. Note that the above formula is valid in the case where the antenna is much smaller than the wavelength [30], i.e. $qd \ll 1$.

Since we wish to study the transmission of the above field through a slab of a number of periodic planes of spheres, it is advantageous to transform the field of equation (1) to a basis of plane waves consistent with the 2D periodicity of the planes of spheres. If the linear antenna is placed to the left of the slab (see the calculation setup in figure 1), then the field radiated to the right is incident on the slab and is written as (assuming the center of coordinates is located at the localized source) [31]

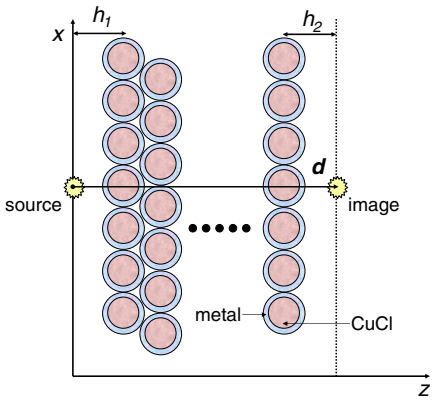

Figure 1. Calculation setup.

$$\mathbf{E}^{\mathrm{inc}+}(\mathbf{r}) = \frac{1}{S_0}\int\int_{\mathrm{SBZ}}\mathrm{d}^2k_\parallel\sum_{\mathbf{g}}\mathbf{E}_{\mathbf{g}}^{\mathrm{inc}+}(\mathbf{k}_\parallel)\exp(\mathrm{i}\mathbf{K}_{\mathbf{g}}^+\cdot\mathbf{r}) \quad (3)$$

with

$$E_{\mathbf{g};i}^{\mathrm{inc}+}(\mathbf{k}_\parallel) = \sum_{l=1}^{\infty}\sum_{m=-l}^{l}\sum_{P=E,H}\Delta_{Plm;i}(\mathbf{K}_{\mathbf{g}}^+)a_{Plm} \quad (4)$$

where $i = 1, 2$ are the two independent polarizations (polar and azimuthal) which are normal to the wavevector [32–34]

$$\mathbf{K}_{\mathbf{g}}^+ = (\mathbf{k}_\parallel + \mathbf{g}, [q^2 - (\mathbf{k}_\parallel + \mathbf{g})^2]^{1/2}). \quad (5)$$

The vectors $\mathbf{g}$ denote the reciprocal-lattice vectors corresponding to the 2D periodic lattice of the plane of spheres and $\mathbf{k}_\parallel$ is the reduced wavevector which lies within the surface Brillouin zone (SBZ) associated with the reciprocal lattice [32–34]. When $q^2 < (\mathbf{k}_\parallel + \mathbf{g})^2$, the wavevector of equation (5) defines an evanescent wave. The coefficients $\boldsymbol{\Delta}_{Plm}$ are given by

$$\begin{aligned}\boldsymbol{\Delta}_{Elm}(\mathbf{K}_{\mathbf{g}}^+) = {} & \frac{2\pi(-\mathrm{i})^l}{qA_0K_{\mathbf{g}z}^+\sqrt{l(l+1)}} \\ & \times\left\{\mathrm{i}[\alpha_l^{-m}\,\mathrm{e}^{\mathrm{i}\phi}\;Y_l^{m-1}(\hat{\mathbf{K}}_{\mathbf{g}}^+) - \alpha_l^m\,\mathrm{e}^{-\mathrm{i}\phi}\;Y_l^{m+1}(\hat{\mathbf{K}}_{\mathbf{g}}^+)]\hat{\mathbf{e}}_1\right. \\ & - [\alpha_l^{-m}\cos\theta\,\mathrm{e}^{\mathrm{i}\phi}\;Y_l^{m-1}(\hat{\mathbf{K}}_{\mathbf{g}}^+) - m\sin\theta\;Y_l^m(\hat{\mathbf{K}}_{\mathbf{g}}^+) \\ & \left.+\,\alpha_l^m\cos\theta\,\mathrm{e}^{-\mathrm{i}\phi}\;Y_l^{m+1}(\hat{\mathbf{K}}_{\mathbf{g}}^+)]\hat{\mathbf{e}}_2\right\}, \end{aligned} \quad (6)$$

$$\begin{aligned}\boldsymbol{\Delta}_{Hlm}(\mathbf{K}_{\mathbf{g}}^+) = {} & \frac{2\pi(-\mathrm{i})^l}{qA_0K_{\mathbf{g}z}^+\sqrt{l(l+1)}}\left\{[\alpha_l^{-m}\cos\theta\,\mathrm{e}^{\mathrm{i}\phi}\;Y_l^{m-1}(\hat{\mathbf{K}}_{\mathbf{g}}^+)\right. \\ & - m\sin\theta\;Y_l^m(\hat{\mathbf{K}}_{\mathbf{g}}^+) + \alpha_l^m\cos\theta\,\mathrm{e}^{-\mathrm{i}\phi}\;Y_l^{m+1}(\hat{\mathbf{K}}_{\mathbf{g}}^+)]\hat{\mathbf{e}}_1 \\ & \left.+\,\mathrm{i}[\alpha_l^{-m}\,\mathrm{e}^{\mathrm{i}\phi}\;Y_l^{m-1}(\hat{\mathbf{K}}_{\mathbf{g}}^+) - \alpha_l^m\,\mathrm{e}^{-\mathrm{i}\phi}\;Y_l^{m+1}(\hat{\mathbf{K}}_{\mathbf{g}}^+)]\hat{\mathbf{e}}_2\right\}, \end{aligned}$$

where θ, ϕ denote the angular variables $(\hat{\mathbf{K}}_{\mathbf{g}}^+)$ of $\mathbf{K}_{\mathbf{g}}^+$ and A_0 is the area of the unit cell of the 2D lattice occupied by the

spheres. Y_l^m denotes a spherical harmonic as usual, $\hat{\mathbf{e}}_1$, $\hat{\mathbf{e}}_2$ are the polar and azimuthal unit vectors, respectively, which are perpendicular to $\mathbf{K}_\mathbf{g}^+$. α_l^m are given by $\alpha_l^m = \frac{1}{2}[(l-m)(l+m+1)]^{1/2}$. The incident field of equation (3) will be partly transmitted through the slab under study. The transmitted field will be given by

$$\mathbf{E}^{\mathrm{tr}+}(\mathbf{r}) = \frac{1}{S_0}\int\int_{\mathrm{SBZ}} \mathrm{d}^2k_\parallel \sum_{\mathbf{g}} \mathbf{E}_\mathbf{g}^{\mathrm{tr}+}(\mathbf{k}_\parallel)\exp[\mathrm{i}\mathbf{K}_\mathbf{g}^+\cdot(\mathbf{r}-\mathbf{d})] \quad (7)$$

with

$$E_{\mathbf{g};i}^{\mathrm{tr}+}(\mathbf{k}_\parallel) = \sum_{\mathbf{g}',i'} Q^I_{\mathbf{g}i;\mathbf{g}'i'} E^{\mathrm{inc}+}_{\mathbf{g}'i'}(\mathbf{k}_\parallel) \quad (8)$$

$\mathbf{d}$ is a vector joining the source to the image (see figure 1). The transmission matrix $\mathbf{Q}^I$ appearing in equation (8) is calculated within the framework of the layer-multiple-scattering method which is an efficient computational method for the study of the electromagnetic (EM) response of 3D photonic structures consisting of non-overlapping spheres [32–34] and axisymmetric non-spherical particles [35]. The layer-multiple-scattering method is ideally suited for the calculation of the transmission, reflection and absorption coefficients of an EM wave incident on a composite slab consisting of a number of layers which can be either planes of non-overlapping particles with the same 2D periodicity or homogeneous plates. For each plane of particles, the method calculates the full multipole expansion of the total multiply scattered wave field and deduces the corresponding transmission and reflection matrices in the plane-wave basis. The transmission and reflection matrices of the composite slab are evaluated from those of the constituent layers. By imposing periodic boundary conditions one can also obtain the (complex) frequency band structure of an infinite periodic crystal. The method applies equally well to non-absorbing systems and to absorbing ones. Its chief advantage over the other existing numerical methods lies in its efficient and reliable treatment of systems containing strongly dispersive materials such as Drude-like and polaritonic materials.

The calculation of the incident (equation (3)) as well as the transmitted field (equation (7)), requires a numerical integration over the entire SBZ. In the example examined in the next section, the spheres in all planes occupy the sites of a square lattice and, therefore, the SBZ is also a square. The SBZ integration of equations (3) and (7) is performed by subdividing progressively the SBZ into smaller and smaller squares, within which a nine-point integration formula [36] is very efficient. Using this formula we managed excellent convergence with a total of 73 728 points in the SBZ. Also, the inclusion of 13 reciprocal-lattice $\mathbf{g}$-vectors along with an angular-momentum cutoff $l_{\max} = 4$ provided converged results.

3. Results

3.1. Description of the metamaterial

We consider a 3D array of closed-packed CuCl nanoparticles of radius $S = 28$ nm; CuCl exhibits a Z_3 exciton line at 386.93 nm [37]. Around the exciton frequency, the dielectric function of the above semiconductor is given by

$$\epsilon_{\mathrm{s}}(\omega) = \epsilon_\infty + A\gamma/(\omega_0 - \omega - \mathrm{i}\gamma). \quad (9)$$

The constant A is proportional to the exciton oscillator strength and for CuCl, $A = 632$. The rest of the parameters for CuCl are [37]: $\epsilon_\infty = 5.59$, $\hbar\omega_0 = 3.363$ eV, and $\hbar\gamma = 5\times10^{-5}$ eV. The small value of the loss factor γ implies a very narrow exciton linewidth. The magnetic permeability μ_{s} of CuCl is unity. Arrays of CuCl nanoparticles (NPs) can be fabricated by colloidal crystallization [38] and ion implantation techniques [39]. The CuCl NPs are coated with a metal of nanometer thickness, $\ell = 0.10S = 2.8$ nm (nanoshell). Such hybrid metal–semiconductor nanoparticles have already been synthesized in the laboratory (for a recent review see [40]). The dielectric function of the metal is assumed to be described by the Drude model, i.e.

$$\epsilon_m = 1 - \frac{\omega_{\mathrm{p}}^2}{\omega(\omega+\mathrm{i}\gamma)}. \quad (10)$$

In order to achieve NRI, ω_{p} is taken to be $\omega_{\mathrm{p}} = 1.05\omega_0$. For the loss factor γ we have taken a typical value of $\gamma/\omega_{\mathrm{p}} = 0.01$ [8]. We note that the plasma frequency ω_{p} of the metal can be easily tuned to the above value if one covers the CuCl core with inhomogeneous metals such as nanoparticulate coatings. For very thin nanoparticulate metal films below the percolation threshold, the plasma frequency is a function of the film thickness [41]. For silver films of thickness of about 3 nm (the proposed thickness of our metallic nanoshell is 2.8 nm), the measured plasma frequency is around 3.3 eV (see figure 6 of [41]) which is very close to the desired value ($\hbar\omega_{\mathrm{p}} = 1.05\hbar\omega_0 = 3.52$ eV) of our metamaterial.

3.2. Dispersion relations and NRI

The effective permittivity ϵ_{eff} and permeability μ_{eff} of such a structure can be calculated by the extended Maxwell–Garnett (EMG) theory [42, 43] which encompasses elements of the Mie theory within the formulas of the ϵ_{eff}, μ_{eff}. As such, the EMG theory agrees very well with more rigorous approaches [8–10, 13, 14]. Figure 2(a) shows the real and imaginary parts of ϵ_{eff}, μ_{eff}, and n_{eff} for the above described system of metal-coated CuCl nanoparticles. One clearly observes a region of negative $\mathrm{Re}\,\epsilon_{\mathrm{eff}}$ for $\omega/\omega_0 < 1.0015$. One can also identify a narrow frequency region around $\omega/\omega_0 \sim 0.9998$, where $\mathrm{Re}\,\mu_{\mathrm{eff}} < 0$ which is entirely within the region of negative $\mathrm{Re}\,\epsilon_{\mathrm{eff}}$. Within this region, $\mathrm{Re}\,n_{\mathrm{eff}} < 0$ and an NRI band occurs. Note that for the calculation of the n_{eff} the imaginary parts of ϵ_{eff}, μ_{eff} have been also taken into account by choosing the branch of $n_{\mathrm{eff}} = \sqrt{\epsilon_{\mathrm{eff}}\mu_{\mathrm{eff}}}$ which corresponds to the positive imaginary part (the structures under study are made from passive materials).

It is worth noting that the selected material and geometric parameters provide an optimized metamaterial. First of all, the close-packed arrangement (volume filling fraction $f = 0.74$) of the spheres ensures the occurrence of negative μ_{eff} which is absent for smaller values of f. The spheres are large enough

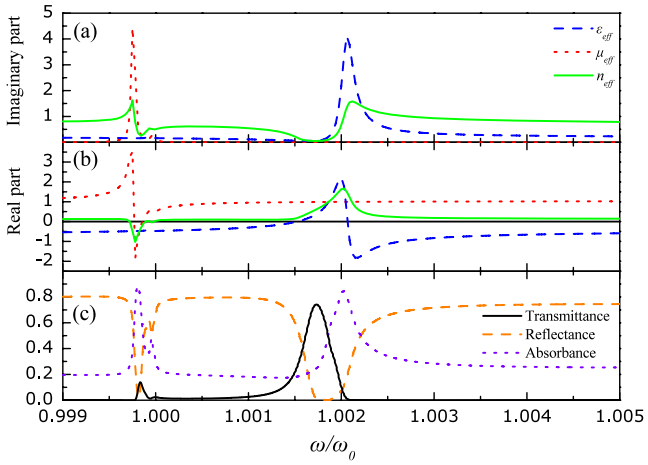

Figure 2. The imaginary (a) and real (b) parts of the effective parameters $n_{\rm eff}$ (solid line), $\epsilon_{\rm eff}$ (dashed line) and $\mu_{\rm eff}$ (dotted line) for a 3D array of close-packed metal-coated CuCl spheres of radius $S = 28$ nm and coating thickness $\ell = 2.8$ nm. (c) Transmittance (solid line), reflectance (dashed line) and absorbance (dotted line) of light incident normally on a slab consisting of four (001) fcc planes of the above nanospheres, as calculated by the layer-multiple scattering method [32–34].

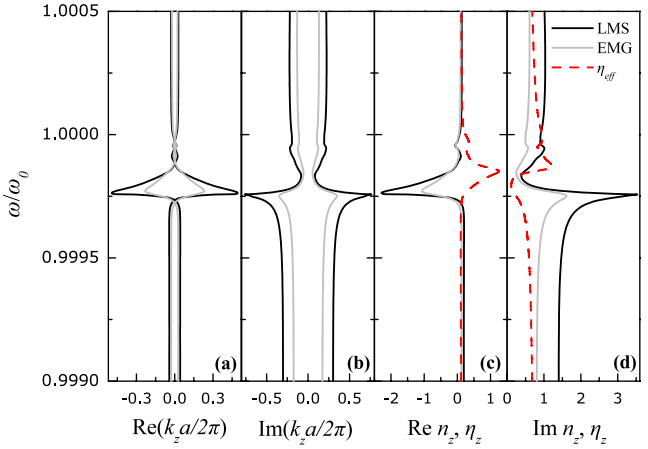

Figure 3. (a) and (b) The black lines depict the complex frequency band structure normal to the (001) surface of an fcc crystal of close-packed metal-coated CuCl spheres ($S = 28$ nm, $\ell = 2.8$ nm) in air, as calculated by the rigorous LMS method. The gray lines show the dispersion curves of the above crystal as obtained from the EMG theory. (c) Real and (d) imaginary parts of the effective refractive index as obtained from the LMS method (black lines) and EMG theory (gray lines). The dashed lines correspond to the impedance $\eta_{\rm eff}$ obtained from the EMG theory.

($S = 28$ nm) to provide negative $\mu_{\rm eff}$ but, at the same time, they are small enough to preserve the subwavelength property of the structure [44]. Furthermore, the plasma frequency $\omega_{\rm p}$ as well as the thickness ℓ of the nanoshell are properly chosen in order to have the widest possible NRI band. For greater values of $\omega_{\rm p}$ and/or ℓ, the overlap of the negative $\epsilon_{\rm eff}$ and $\mu_{\rm eff}$ regions diminishes and the NRI band is eventually lost.

In order to verify the validity of the effective medium parameters depicted in figures 2(a) and (b) we have also employed the layer-multiple scattering (LMS) method [32–34] (briefly outlined in section 2) in order to calculate the transmittance of light incident normally on a finite slab of an fcc crystal of the above nanospheres as well as the complex frequency band structure. We have chosen the fcc lattice since this type of lattice can satisfy a close-packed arrangement of spheres. The slab consists of four (001) fcc planes of nanospheres and the respective transmittance is shown in figure 2(c). It is evident that within the NRI band of figure 2(b), the transmittance shows a maximum which is what one expects from a slab of NRI [19]. As light propagates through the slab, it is also attenuated due to the intrinsic losses of the constituent materials (CuCl and Drude-metal) as is evident from the corresponding maximum of the absorbance curve of figure 2(c) within the NRI band. It is also evident that there is a wider transmittance peak from $\omega/\omega_0 \simeq 1.0015$ to 1.002 which, however, corresponds to a region of refractive index with positive real part (the matching of these two frequency regions is not perfect since figure 2(a) is based on an effective medium approximation whilst figure 2(b) is from an exact theory). In between these peaks as well as above the second peak, the transmittance is suppressed as only one of Re $\epsilon_{\rm eff}$ and Re $\mu_{\rm eff}$ becomes negative, giving rise to a practically imaginary refractive index (see figures 2(a) and (b)).

We further compare the EMG results with the rigorous LMS method, in figure 3. The black lines in figures 3(a) and (b) depict the complex frequency band structure normal to the (001) surface of fcc, around the NRI band, as obtained from the LMS method. We note that due to the presence of losses in the metamaterial under study, we depict the frequency band which corresponds to the smallest Im k_z since the latter determines the rate of attenuation of an incident wave within the metamaterial slab. The LMS complex frequency band structure is compared against the EMG dispersion relation $k = (\omega/c)\sqrt{\epsilon_{\rm eff}(\omega)\mu_{\rm eff}(\omega)}$ where $\epsilon_{\rm eff}$ and $\mu_{\rm eff}$ are those of figures 2(a) and (b). Figures 3(c) and (d) show the refractive index as deduced from the LMS complex frequency band structure and the corresponding EMG refractive index. From all these curves it is evident that there is an overall good agreement between the effective medium theory and the first-principles treatment. There is only some significant difference in the dip value of the refractive index. Figures 3(c) and (d) also show the real and imaginary parts of the impedance $\eta_{\rm eff}$ as calculated by the EMG theory. A similar quantity cannot be obtained from the LMS frequency band structure since one cannot separately determine $\epsilon_{\rm eff}$ and $\mu_{\rm eff}$.

3.3. Imaging properties

According to the effective medium theory for a lossless metamaterial lens [3], perfect imaging is achieved when the refractive index of the metamaterial slab is minus unity (if the slab is surrounded by air) and the corresponding impedance is equal to plus unity. But, even when there is complete index and impedance mismatch between a NRI material and air, paraxial beams will still focus to a point [45]. In this latter case, however, the image is distorted as the inhomogeneous components are not perfectly transferred [45]. In our case, the metamaterial under study is lossy and, therefore, the imaging conditions of [45] are never met, resulting in a distorted final

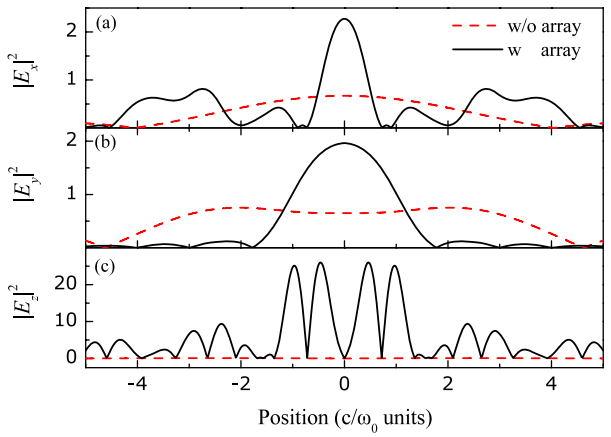

Figure 4. Distribution of $|E_x|^2$ (a), $|E_y|^2$ (b), and $|E_z|^2$ (c) (in arbitrary units) along the line $y = 0$ in the plane lying at a distance $h_2 = 0.6c/\omega_0$ from the plane of spheres (see figure 1), for frequency $\omega/\omega_0 = 0.999\,84$. The solid lines refer to the field distribution from a localized source (antenna) placed at a distance $h_1 = 0.6c/\omega_0$ from the center of a single plane of close-packed metal-coated CuCl nanospheres (see figure 1). The dashed lines refer to the free-space case (no spheres present).

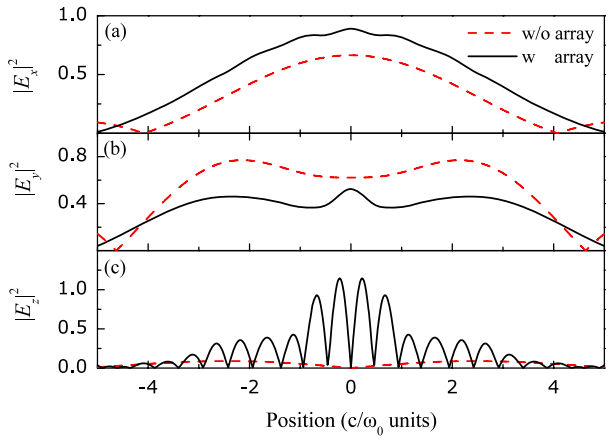

Figure 5. Same as in figure 3 but for frequency $\omega/\omega_0 = 1.001\,68$.

image. However, subwavelength imaging (though not perfect) can still be feasible provided that the NRI slab is much smaller than the working wavelength [46].

Therefore, in order to probe the subwavelength imaging properties of the metamaterial under study, we have applied the formalism developed in section 2 for the case of a *single* plane of metal-coated CuCl nanospheres. As a localized source of light we have considered a linear, infinitely thin, center-fed antenna of width $d = 0.001c/\omega_0$, lying along the z-axis. It is placed at a distance $h_1 = 0.6c/\omega_0$ from the center of a single plane of spheres (see figure 1). This particular choice of light source is justified by the fact that the proposed optical LHM can be easily realized in the infrared or even in the microwave regime, e.g. by using phonon–polaritonic resonances (instead of excitonic ones) in order to provide negative $\mu_{\rm eff}$ and consequently NRI [8, 44]. In these regimes, the type of antenna described above is a realistic choice of radiation source.

Figure 4 shows the distribution of all three electric-field components along the line $y = 0$ in a plane lying at a distance $h_2 = 0.6c/\omega_0$ from the plane of spheres (see figure 1), for frequency $\omega/\omega_0 = 0.999\,84$ corresponding to the low-frequency maximum of the transmittance curve of figure 2(c). Since we cannot retrieve $\epsilon_{\rm eff}$, $\mu_{\rm eff}$ and hence the impedance directly from the complex frequency band structure of figure 3 (LMS method), we have chosen this particular frequency (corresponding to maximum transmittance within the NRI band) in order to maximize, at least, the transfer of the propagating components. For comparison, we also show the corresponding curves in the absence of the plane of spheres. We note that the field distributions of all figures that follow contain both the far-field ($q^2 > (\mathbf{k}_\parallel + \mathbf{g})^2$ in equation (5)) and near-field ($q^2 < (\mathbf{k}_\parallel + \mathbf{g})^2$ in equation (5)) components. Since the chosen frequency ($\omega/\omega_0 = 0.999\,84$) lies within the NRI band of the array of spheres (see above), we expect that the near-field components which are transmitted through the plane will be amplified. And this is indeed what we observe in figure 4. We observe that *all* three components of the electric-field are amplified with respect to the case where the plane of spheres is absent. This can occur only in the case of NRI where, as predicted by Pendry [3], both polarization modes are amplified when transmitted through a planar NRI slab. We remember that when only one of $\epsilon_{\rm eff} < 0$ or $\mu_{\rm eff} < 0$ occurs, the near-field amplification affects one of the polarization modes [23–27]. In addition to the near-field amplification of the electric-field, we observe that the full width at half minimum (FWHM) for the E_x- ($\sim\lambda_0/7$) and E_y- components ($\sim\lambda_0/3$) is considerably smaller than the free-space case, suggesting a subwavelength imaging operation of the structure (see below). The E_z-component (figure 4(c)) is much more amplified than the other two; however, the field distribution looks much more complicated, possibly, due to interference effects (the far-field is also included in the calculation) and the peculiarity of the source (the E_z-component emitted by a center-fed antenna possesses a nodal line along the direction of the antenna axis).

In order to confirm the fact that the near-field amplification shown in figure 4 is attributed to the occurrence of NRI, in figure 5 we show the same quantities, for the same calculation setup as in figure 4, but for frequency $\omega/\omega_0 = 1.001\,68$ corresponding to the high-frequency transmission peak of figure 2(c), which lies out of the NRI band. We observe that only the E_z-component (figure 5(c)) shows a similar trend to that of figure 4(c). The E_y-component is suppressed compared to the free-space case whilst the E_x-component is barely amplified from the plane of nanospheres. Also, the subwavelength profile of the field distributions is lost as the maxima are almost as wide as those of the free-space case. So, judging from figure 5, we can infer that the field amplification for all polarizations and the subwavelength width of the electric-field of figure 4 are in accordance with the occurrence of NRI.

Figure 6 shows the image of the center-fed antenna for different values of the refractive index as obtained by the LMS method (figures 3(c) and (d)). The value $n = -0.38 + i0.4$ corresponds to the case of figure 4 (frequency of maximum

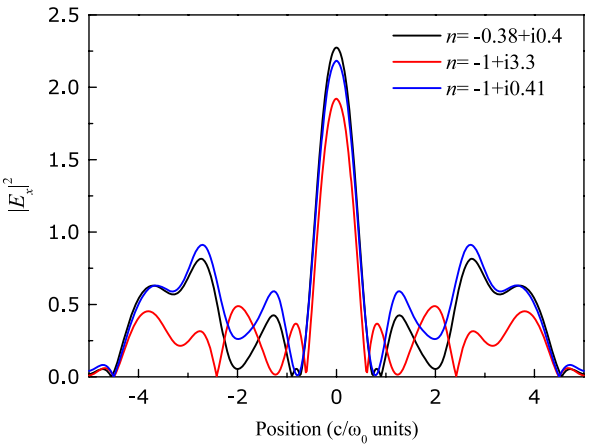

Figure 6. Distribution of $|E_x|^2$ (in arbitrary units) along the line $y = 0$ and at distance $h_2 = 0.6c/\omega_0$ from a single plane of spheres (see figure 1), for different values of the refractive index (see legend) as obtained by the LMS method. The source (antenna) is placed at a distance $h_1 = 0.6c/\omega_0$ from the plane of spheres.

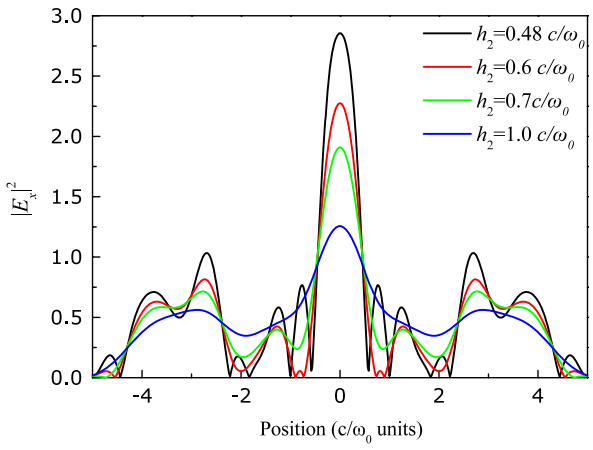

Figure 7. Distribution of $|E_x|^2$ (in arbitrary units) for frequency $\omega/\omega_0 = 0.999\,84$, along the line $y = 0$ and for various distances h_2 (see legend) from the plane of spheres. The source (antenna) is placed at distance $h_1 = 0.6c/\omega_0$ from the plane of spheres.

transmittance within the NRI band). The other two curves correspond to the real part of n, $\mathrm{Re}\,n = -1$. We observe that for $n = -1 + \mathrm{i}3.3$ the amplification is smaller than for $n = -1 + \mathrm{i}0.41$ due to the much higher value of $\mathrm{Im}\,n$. However, the peak value of the field for $n = -1 + \mathrm{i}3.3$ is not much smaller than that of $n = -1 + \mathrm{i}0.41$ since the critical wavevector above which the image transfer function diminishes is linearly proportional to the *logarithm* of the imaginary part of the refractive index [46].

We note that the formulas for the position of the focal point as given in [45] cannot be met by our lossy LHM metamaterial. Therefore, we proceed numerically to locate the position of the image plane. Figure 7 shows the transmitted field intensity for different distances h_2 from the plane of spheres. It is evident that the maximum of the central peak occurs for $h_2 = 0.48c/\omega_0$, i.e. the image plane is the plane which is tangential to the spheres. This would imply that the propagating beams cannot be focused to a point due to the high amount of losses in the LHM slab.

Next, in figure 8, we probe the imaging properties of thicker slabs, i.e. slabs containing more than one plane of nanospheres. We have chosen to depict the E_x-component but similar effects are observed for the other two components. For the case of two planes of nanospheres (figure 8(a)), the field amplification is still evident although somewhat distorted at the center. There are also two satellite peaks evident which may influence a potential imaging operation of the structure. For a three-plane-thick slab (figure 8(b)) the amplification of the transmitted field is not as dramatic as for thinner slabs (figures 4(a) and 8(a)) whilst for the four-plane-thick slab the amplification is evidently lost. At first glance, this seems to be an unexpected result: the extended Maxwell–Garnett theory [42, 43] which was employed for the calculation of n_{eff} in figures 2(a) and (b) refers to 3D collections of scatterers and it is supposed to be more applicable to thick enough slabs. However, as both constituent materials of the nanospheres (metal and semiconductor) suffer from losses (especially the

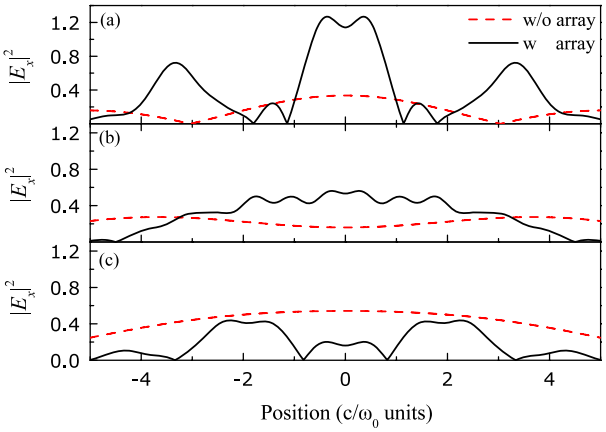

Figure 8. Solid lines: distribution of $|E_x|^2$ (in arbitrary units) along the line $y = 0$ in the plane lying at a distance $h_2 = 0.6c/\omega_0$ from the plane of spheres (see figure 1), for frequency $\omega/\omega_0 = 0.999\,84$, in the presence of a slab consisting of two (a), three (b) and four (c) planes of close-packed metal-coated CuCl nanospheres. The distance of the source from the center of the left plane of the slab is $h = 0.6c/\omega_0$. The dashed lines refer to the free-space case (no spheres present).

metal) we expect that thicker slabs mean longer optical paths for the transmitted field, and, therefore, higher losses which counterbalance the near-field amplification effect. This is also manifested in figure 2(c) where almost 90% of the incident power is absorbed within the slab (of four planes of spheres). Similar effects have also been measured experimentally for LHMs in the microwave regime [22]. The results of figure 8 are in agreement with previous suggestions [46], namely that in order to accomplish near-field amplification in a lossy LHM, the slab thickness must be much smaller than the wavelength. This is why the most efficient amplification occurs for a single plane of spheres where the thickness is $D = 2S \cong \lambda/6.5$. For comparison, the thickness for the slab of four planes is $D \cong \lambda/1.6$.

Finally, in order to study the image-resolution properties of the array of nanospheres, in figure 9, we have considered

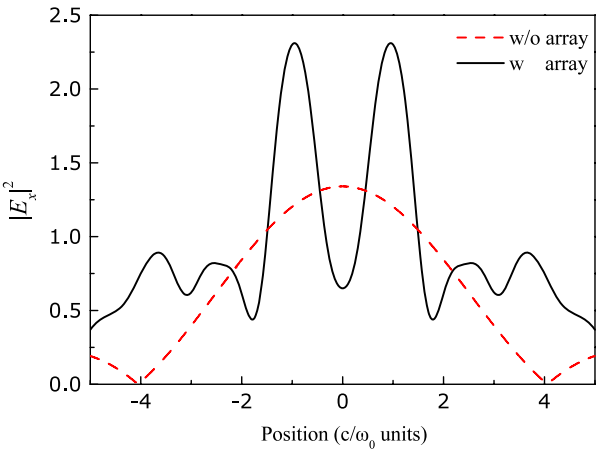

Figure 9. Field distribution for two sources separated by distance $c/\omega_0 = \lambda_0/\pi$ and arranged symmetrically with respect to the center of a sphere of a single plane of close-packed metal-coated CuCl nanospheres (solid lines). The sources are placed at a distance $h_1 = 0.6c/\omega_0$ from the center of a single sphere of the plane. The dashed lines refer to the free-space case (no spheres present).

the case of two localized sources (small center-fed antennas) separated by a vertical subwavelength distance of $c/\omega_0 = \lambda_0/\pi$. The array consists of a single plane of nanospheres since absorption is expected to make the image resolution deteriorate for thicker slabs. The sources are placed symmetrically with respect to the center of a sphere, at a distance $h_1 = 0.6c/\omega_0$ from the plane. As is evident from the dashed curve of figure 9, the distance between the sources is too small to be resolved in free-space (a single peak appears). However, in the presence of the plane of nanospheres, the occurrence of NRI is accompanied by a dramatic increase in the image resolution, which allows for distinguishing the two sources in space by use of visible light. We note that the image resolution can be further improved by using smaller nanospheres, down to a radius of 15 nm. However, for CuCl spheres smaller than that, μ_{eff} is no longer negative [44] around the exciton resonance and a NRI band is not expected to occur.

4. Conclusion

It has been shown that arrays of metal-coated semiconductor nanospheres can exhibit NRI around the exciton resonance (if such exists) of the semiconductor. The existence of NRI has been studied by use of the extended Maxwell–Garnett theory and confirmed by rigorous EM calculations of light transmittance. Within the NRI band, an array of such spheres can amplify the near-field for both polarization modes, in accordance with Pendry's theory [3]. The near-field amplification is accompanied by subwavelength image resolution that is only limited by the inherent losses of the metal and the semiconductor. The systems studied in this work are strong candidates for LHMs in the optical regime due to their fabrication with existing methods of colloidal chemistry [38–40, 47].

References

[1] Lakhtakia A and Mackay T G 2007 *Opt. Photon. News* **18** 32
[2] Veselago V G 1968 *Sov. Phys.—Usp.* **10** 509
[3] Pendry J B 2000 *Phys. Rev. Lett.* **85** 3966
[4] Eleftheriades G V and Balmain K G (ed) 2005 *Negative-Refraction Metamaterials* (New Jersey: Wiley)
[5] O'Brien S and Pendry J B 2002 *J. Phys.: Condens. Matter* **14** 4035
[6] Holloway C L, Kuester E F, Baker-Jarvis J and Kabos P 2003 *IEEE Trans. Antennas Propag.* **51** 2596
[7] Huang K C, Povinelli M L and Joannopoulos J D 2004 *Appl. Phys. Lett.* **85** 543
[8] Yannopapas V and Moroz A 2005 *J. Phys.: Condens. Matter* **17** 3717
[9] Wheeler M S, Aitchison J S and Mojahedi M 2005 *Phys. Rev.* B **72** 193103
[10] Wheeler M S, Aitchison J S and Mojahedi M 2005 *Phys. Rev.* B **73** 045105
[11] Jylhä L, Kolmakov I, Maslovski S and Tretyakov S 2006 *J. Appl. Phys.* **99** 043102
[12] MacKay T G and Lakhtakia A 2006 *J. Appl. Phys.* **100** 063533
[13] Yannopapas V and Vitanov N V 2006 *Phys. Rev.* B **74** 193304
[14] Yannopapas V 2007 *Phys. Rev.* B **75** 035112
[15] Peng L, Ran L, Chen H, Zhang H, Kong J A and Grzegorczyk T M 2007 *Phys. Rev. Lett.* **98** 157403
[16] Schuller J A, Zia R, Taubner T and Brongersma M L 2007 *Phys. Rev. Lett.* **99** 107401
[17] Redl F X, Cho K-S, Murray C B and O'Brien S 2003 *Nature* **423** 968
Saunders A E and Korgel B A 2005 *ChemPhysChem* **6** 61
Shevchenko E V, Talapin D V, Kotov N A, O'Brien S and Murray C B 2006 *Nature* **439** 55
Kalsin A M, Fialkowski M, Paszewski M, Smoukov S K, Bishop K J M and Grzybowski B A 2006 *Science* **312** 420
[18] Parazzoli C G, Greegor R B, Li K, Koltenbah B E C and Tanielian M 2003 *Phys. Rev. Lett.* **90** 107401
[19] Houck A A, Brock J B and Chuang I L 2003 *Phys. Rev. Lett.* **90** 137401
[20] Lagarkov A N and Kissel V N 2004 *Phys. Rev. Lett.* **92** 077401
[21] Grbic A and Eleftheriades G 2004 *Phys. Rev. Lett.* **92** 117403
[22] Aydin K, Bulu I and Ozbay E 2007 *Appl. Phys. Lett.* **90** 254102
Ozbay E and Aydin K 2008 *Photon. Nanostruct.-Fundam. Appl.* **6** 108
[23] Wiltshire M C K, Pendry J B, Young I R, Larkman D J, Gilderdale D J and Hajnal J V 2001 *Science* **291** 849
[24] Wiltshire M C K, Pendry J B and Hajnal J V 2006 *J. Phys.: Condens. Matter* **18** L315
[25] Ono A, Kato J and Kawata S 2005 *Phys. Rev. Lett.* **95** 267407
[26] Fedorov G, Maslovski S I, Dorofeenko A V, Vinogradov A P, Ryzhikov I A and Tretyakov S A 2006 *Phys. Rev.* B **73** 035409
[27] Alitalo P, Simovski C, Viitanen A and Tretyakov S 2006 *Phys. Rev.* B **74** 235425
[28] Yannopapas V 2007 *Phys. Status Solidi (RRL)* **1** 208
[29] Jackson J D 1975 *Classical Electrodynamics* (New York: Wiley)
[30] Naus H W L 2007 *Phys. Rev.* E **76** 026602
[31] Modinos A, Yannopapas V and Stefanou N 2000 *Phys. Rev.* B **61** 8099
[32] Stefanou N, Karathanos V and Modinos A 1992 *J. Phys.: Condens. Matter* **4** 7389
[33] Stefanou N, Yannopapas V and Modinos A 1998 *Comput. Phys. Commun.* **113** 49
[34] Stefanou N, Yannopapas V and Modinos A 2000 *Comput. Phys. Commun.* **132** 189
[35] Gantzounis G and Stefanou N 2006 *Phys. Rev.* B **73** 035115
[36] Abramowitz M and Stegun I A 1965 *Handbook of Mathematical Functions* (New York: Dover)

[37] Artoni M, La Rocca G and Bassani F 2005 *Phys. Rev.* E **72** 046604
[38] Orel Z C, Matijević E and Goia D V 2003 *Colloid Polym. Sci.* **281** 754
[39] Fukumi K, Chayahara A, Kageyama H, Kadono K, Akai T, Kitamura N, Mizoguchi H, Horino Y, Makihara M, Fujii K and Hayakawa J 1999 *J. Non-Cryst. Solids* **259** 93
[40] Cozzoli P D, Pellegrino T and Manna L 2006 *Chem. Soc. Rev.* **35** 1195
[41] Oates T W H and Mücklich A 2005 *Nanotechnology* **16** 2606
[42] Doyle W T 1989 *Phys. Rev.* B **39** 9852
[43] Ruppin R 2000 *Opt. Commun.* **182** 273
[44] Yannopapas V 2007 *Appl. Phys.* A **87** 259
[45] Tassin P, Veretennicoff I and Van der Sande G 2006 *Opt. Commun.* **264** 130
[46] Shen L and He S 2003 *Phys. Lett.* A **309** 298
[47] Gaponenko S V, Germanenko I N, Gribkovskii V P, Zimin L G, Lebed V Y and Malinovskii I E 1993 *Physica* B **185** 588